Water Vapor Variability in the Thermosphere of Mars during Mars Years 32-35

Z. Girazian[1]

[1]Department of Physics and Astronomy, University of Iowa, Iowa City, IA, USA

Key Points:

- Water vapor in the thermosphere of Mars varies with season.
- The water abundance is highly correlated with the amount of dust in the lower atmosphere.
- Water densities increase during regional dust storms.

Corresponding author: Zach Girazian, zachary-girazian@uiowa.edu

Abstract

Using Mars Atmosphere and Volatile Evolution observations, we characterize the variability of water vapor in the Martian thermosphere during Mars Years 32-35. Near a fixed atmospheric pressure level of $\sim 5{\times}10^{-7}$ Pa, the typical water density is 1.3 ($\pm$0.8)$\times$ 10^3 cm^{-3} and the typical water mixing ratio is 10 ($\pm$6) ppm. Thermospheric water levels are higher during the southern spring and summer seasons when Mars is near perihelion and there is significant dust loading in the lower atmosphere. However, the seasonal variation is not the same from year-to-year, likely due annual differences in dust loading. Water vapor is highly correlated with lower atmospheric dust, and increases during both regional and global dust storms. Our results support previous work that found increased dust levels allow more water to be supplied directly to the thermosphere.

Plain Language Summary

Water vapor in the atmosphere of Mars can be transported to high altitudes and ultimately lost to space. Hence, understanding the distribution and variability of water throughout the atmosphere is critical for determining the processes that control water loss at Mars. We present new results on the variability of water vapor in the thermosphere of Mars (185 km), a region where few water observations exist. We find there is more water during the southern spring and summer seasons when Mars is closest to the Sun and there is a significant amount of dust in the lower atmosphere. We also find that the amount of water is highly correlated with the amount of dust in the lower atmosphere. These results are consistent with previous studies that have shown atmospheric heating from increased dust levels allows more water to be transported to high altitudes without condensing.

1 Introduction

Water vapor is a common ingredient in the Martian atmosphere, and although it is only a minor constituent, it plays a crucial role in controlling the escape of hydrogen to space. Water is broken apart by ultraviolet sunlight, resulting in H atoms that populate the extended hydrogen exosphere and escape to space via the Jeans mechanism (Hunten & McElroy, 1970; Jakosky, 2021). Hence, understanding the global water cycle is a major theme of research aimed at understanding present-day processes in the atmosphere of Mars, and its evolution through time.

The water vapor is mostly concentrated below $\sim$ 60 km (Aoki et al., 2022) where temperatures are low enough to enable condensation and cloud formation (A. Fedorova et al., 2021), thereby creating a "cold trap" that impedes the upward transport of water. The low-altitude water exhibits a substantial seasonal variation (Montmessin et al., 2017; Aoki et al., 2022). Water abundances peak around perihelion and southern summer (when the solar longitude, L_s, is between 200° and 300°) when stronger solar heating increases the sublimation rate of water frozen in the polar caps (Haberle & Jakosky, 1990; Aoki et al., 2022). This period also coincides with dust storm season, which further heats the atmosphere and allows water to propagate to higher altitudes without condensing. Lower atmospheric water abundances reach a minimum during northern spring (L_s = 0°-90°) when solar heating is weakest and atmospheric dust levels are at their minimum.

The seasonal trends of low-altitude water are also imprinted on the H escape rate which reaches a maximum during the perihelion and southern summer season (Bhattacharyya et al., 2015; Halekas, 2017; Halekas et al., 2018). Additionally, both global and regional dust storms can rapidly increase the amount of water delivered to the upper atmosphere, leading to impulsive events of increased high altitude water and hydrogen escape (M. Chaf-

fin et al., 2017; A. A. Fedorova et al., 2020; A. Fedorova et al., 2021; Villanueva et al., 2021).

Water in the lower and middle atmosphere of Mars has been monitored for several decades (Clancy et al., 1996; A. Fedorova et al., 2006; Smith et al., 2009; A. Fedorova et al., 2021; Crismani et al., 2021). Meanwhile, direct measurements of water vapor at higher altitudes in the thermosphere (100-200 km) have been much more sparse. The most comprehensive study of water vapor in the thermosphere was conducted by Stone et al. (2020) (hereafter, Stone20), who used ion-neutral chemistry to infer water abundances from measurements by the Mars Atmosphere and Volatile Evolution's (MAVEN's) Neutral Gas and Ion Mass Spectrometer (NGIMS) (Mahaffy et al., 2015; Benna et al., 2015). Using the inferred water densities, Stone20 found a seasonal variation in the thermospheric water abundance that mimics the seasonal variation of water in lower atmosphere: thermospheric water levels reach a maximum during perihelion and southern summer (L_s = 259°), and a minimum during northern spring and summer (L_s=86°). Stone20 also found a rapid increase in the thermospheric water abundance during two regional dust storms and during the 2018 global dust storm.

Given the Stone20 study was completed using MAVEN observations obtained between October 2014 and November 2018 (MY32-MY34), we are motivated to extend the analysis with the addition of more recent data. In this study, we use a similar methodology to derive thermospheric water abundances and mixing ratios from NGIMS observations. The newly extended data set includes observational coverage throughout Mars Year 35 (MY35), which was unavailable for the Stone20 study. With the extended data set our study aims to (1) reassess the seasonal cycle of thermospheric water; (2) quantify the dependence of thermospheric water on lower atmospheric dust content, and (3) determine how the thermospheric water abundance responded during two MY35 regional dust storms.

2 Method

NGIMS cannot measure water vapor directly, but measurements of H_3O^+, and knowledge of its ion-neutral chemistry, allow us to calculate the water vapor abundance. This technique was first applied to NGIMS observations by Stone20. We adopt the main aspects of their methodology and what follows is only a brief description of the technique (we refer readers to Stone20 for the full, detailed description). The technique leverages the assumption that injections of water into the thermosphere increase the densities of protonated ion species such as H_3O^+, H_2O^+, HCO^+ (Matta et al., 2013; Fox et al., 2015).

More concretely, in the thermosphere of Mars, H_3O^+ is produced mainly by two chemical reactions, and both involve water:

$$HCO^+ + H_2O \xrightarrow{k_1} H_3O^+ + CO \tag{1}$$

$$H_2O^+ + H_2O \xrightarrow{k_2} H_3O^+ + OH. \tag{2}$$

H_3O^+ is then lost through dissociative recombination:

$$H_3O^+ + e^- \xrightarrow{\alpha_1} OH + H + H \tag{3}$$

$$\xrightarrow{\alpha_2} H_2O + H \tag{4}$$

$$\xrightarrow{\alpha_3} OH + H_2 \tag{5}$$

$$\xrightarrow{\alpha_4} O + H_2 + H. \tag{6}$$

Here, k_n are rate coefficients and α_n are dissociative recombination coefficients. Note the production rate of H_3O^+ is directly proportional to the water vapor abundance (Reactions 1-2). If we assume H_3O^+ is in photochemical equilibrium, then its production rate is equal to its loss rate. Equating the production and loss rates described in Reactions 1-6 results in the equation

$$[H_2O]\left(k_1[HCO^+] + k_2[H_2O^+]\right) = \alpha[H_3O^+][e^-] \tag{7}$$

where brackets indicate abundances, $[e^-]$ is the total electron density, and $\alpha \equiv \alpha_1 + \alpha_2 + \alpha_3 + \alpha_4$. Rearranging Eq. 7 leads to an equation for the water vapor abundance:

$$[H_2O] = \frac{\alpha[H_3O^+][e^-]}{k_1[HCO^+] + k_2[H_2O^+]} \tag{8}$$

The coefficients are $k_1 = 2.5 \times 10^{-9} \left(\frac{300}{T_i}\right)^{0.5}$ cm^3 s^{-1}, $k_2 = 2.1 \times 10^{-9} \left(\frac{300}{T_i}\right)^{0.5}$ cm^3 s^{-1}, and $\alpha = 4.36 \times 10^{-7} \left(\frac{300}{T_e}\right)^{0.5}$ cm^3 s^{-1} where T_i is the ion temperature and T_e is the electron temperature, both in units of Kelvin (McElroy et al., 2013). Since H_2O^+ densities are several orders of magnitude smaller than HCO^+ densities (Benna et al., 2015), Equation 8 can be written as

$$[H_2O] = \frac{\alpha[H_3O^+][e^-]}{k_1[HCO^+]}. \tag{9}$$

Notice the water vapor abundance is proportional to the $[H_3O^+]/[HCO^+]$ density ratio as discussed in Fox et al. (2015).

All of the abundances on the right hand side of Equation 9 are measured by NGIMS and reported in the Level 2 data products (we assume the electron density is equal to the total ion density). The remaining physical quantities are T_e and T_i, which control the reaction rates. For these, we use Level 2 T_e measurements from MAVEN's Langmuir Probe and Waves (LPW) instrument (Andersson et al., 2015; Ergun et al., 2015) and assume $T_i = T_e$, which is a reasonable assumption at the altitudes of interest (Schunk & Nagy, 2009).

Equation 9 is only valid when H_3O^+ is in photochemical equilibrium. This is satisfied at lower altitudes in the thermosphere where the pressure is higher and collisions are more frequent. Stone20 calculated the atmospheric CO_2 density level above which photochemical equilibrium is satisfied. This density level ranges from $\sim 5\times10^6$ cm^{-3} - 5×10^7 cm^{-3}, depending on the conditions. We adopt a conservative approach to ensure photochemical equilibrium is satisfied by only calculating water abundances at CO_2 density levels greater than 5×10^7 cm^{-3} (altitudes below $\sim$ 190 km). We also only consider dayside observations with solar zenith angles (SZAs) $< 80°$.

An example of MAVEN observations used to calculate the water abundance during one orbit is shown in Figure 1. The measurements are from the inbound leg of the orbit at 8:30 UTC on 2015-Oct-10. The water abundance profile, derived using the measured quantities and Equation 9, is also shown; it only extends up to 183 km (where the CO_2 density drops below 5×10^7 cm^{-3}) to ensure H_3O^+ photochemical equilibrium is satisfied and Equation 9 is valid. The uncertainties of the derived water abundances are assumed to be 70% as estimated by Stone20. Although not shown, the water volume mixing ratio for each orbit is also calculated by dividing the water abundances by the total neutral density measured by NGIMS.

As seen in Figure 1, the H_3O^+ densities can be very small ($\leq 10^{-1}$ cm^{-3}). So small that NGIMS often only registers one or two counts, leading to a high uncertainty in the measured ion density. We mitigate this issue by removing all H_3O^+ densities below a threshold of $1.0{\times}10^{-1}$ cm^{-3}. This threshold was determined by inspection of the NGIMS Level 1b files, which contain count levels; it roughly corresponds to the threshold above which there are more than ~2 counts.

To derive our final data product for an orbit, we calculate the median water density and mixing ratio at a CO_2 density level between 5×10^7 cm^{-3} to 1×10^8 cm^{-3}. This roughly corresponds to a fixed atmospheric pressure level of 5×10^{-7} Pa and an altitude of 185 km. Using this procedure, the water abundance and mixing ratio reported for the orbit shown in Figure 1 are, respectively, $1.8(\pm1.3){\times}10^3$ cm^{-3} and 20.0(±14.0). The median values from each orbit are assigned SZAs, latitudes, longitudes, and local times by averaging the quantity of interest over the same CO_2 density range.

Using this procedure, we derive water abundances and mixing ratios for 1608 orbits using observations from 2015-Jan-1 to 2022-Feb-17. From 2014-2018, MAVEN was in a 4.5 hour elliptical orbit with a periapsis altitude near 160 km. The spacecraft underwent an aerobraking campaign in early 2019 that changed the orbital period to 3.5 hrs and raised the periapsis altitude. For an orbit to be used in our analysis it must contain both neutral and ion measurements from NGIMS. Only the inbound segment of each orbit is used to ensure the NGIMS background level is small (Stone et al., 2018). We also remove any observations obtained when the spacecraft potential was less than -4 volts, which can cause NGIMS to make erroneous measurements.

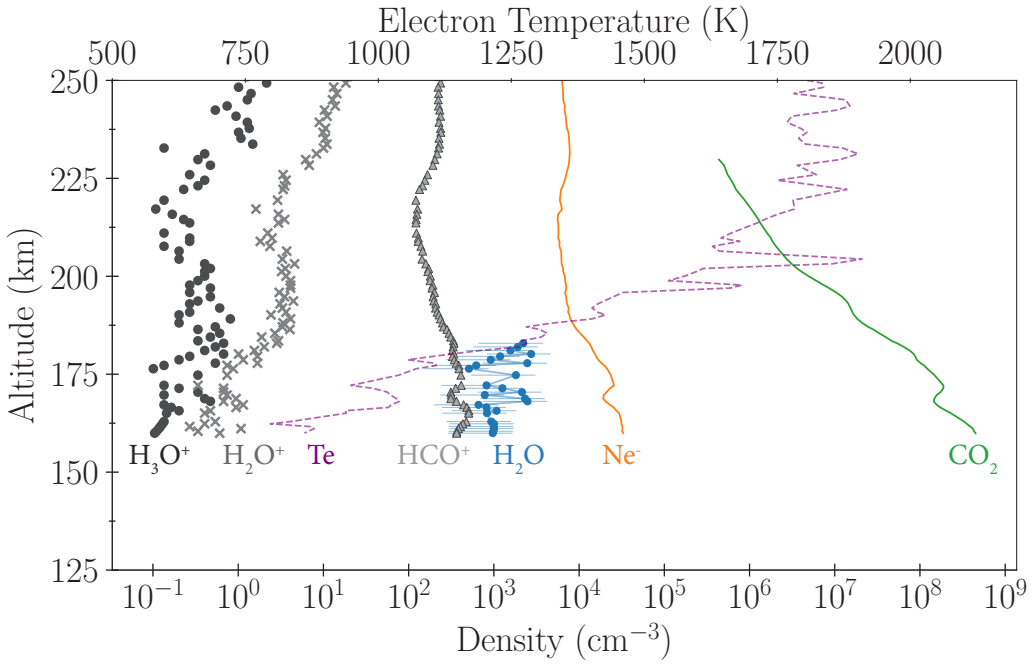

Figure 1. Density and temperature profiles measured by MAVEN on 2015-Oct-10 at 8:30 UTC. The water vapor profile (blue) is derived from Equation 9 using the densities measured by NGIMS and the electron temperatures measured by LPW. The water vapor profile only extends up to 183 km because Equation 9 is only valid at altitudes where H_3O^+ is in photochemical equilibrium.

We also use dust optical depth maps from Montabone et al. (2015) and (Montabone et al., 2020), which are compiled from dust observations by instruments across several Mars missions. The maps provide a continuous measure of the amount of dust in the lower atmosphere, with near-global coverage. Specifically, the maps provide a continuous record of the optical depth of atmospheric absorption at a wavelength of 9.3 μm, normalized to an atmospheric pressure level of 610 Pa (also called the "column dust optical depth"). The maps are regularly gridded and have complete global coverage (missing locations are estimated using an interpolation technique). We assign a global average dust optical depth to each orbit by averaging the global dust map that is closest in time to the observation. This provides a measure of the lower atmospheric dust content for each water measurement.

The top two panels in Figure 2 show the complete set of derived water abundances and mixing ratios, with data points colored by local time of the observation. The large data gaps are primarily from times when MAVEN's periapsis was on the nightside and Equation 9 cannot be used to derive water densities. The bottom panel in Figure 2 shows the time series of global dust optical depth maps with red tracks marking the latitudes of the MAVEN observations.

3 Results

3.1 Overview

Our derived mixing ratios are systematically larger (by a factor of ∼3) than those derived by Stone20. This discrepancy is primarily caused by the different altitude ranges used to derive the water abundances and mixing ratios. In Stone20, they calculate the values near periapsis, which can vary from ∼150-180 km throughout the mission. We, instead, calculate them at a fixed CO_2 density level which corresponds to higher altitudes around 185 km. At these higher altitudes the atmospheric density is much lower, resulting in increased mixing ratios. Nonetheless, the variations in our derived mixing ratios match well with Stone20. Further, as a check, we calculated mixing ratios near periapsis and derived values consistent with those found by Stone20. Some minor differences between our derived values are also present because of our slightly different methods. In particular, we use measured electron temperatures while Stone20 assumed the electron temperature was equal to the neutral temperature.

As an ensemble, the derived water abundances are consistent with a log-normal distribution (with a high end tail). The average (and standard deviation) of the $\log_{10}$ of the water abundances is 3.1 ($\pm$0.3). This corresponds to an average abundance of 1.3 ($\pm$0.8) $\times 10^3$ cm^{-3}. For the $\log_{10}$ of the mixing ratio, the average is 1.0 ($\pm$0.3) which corresponds to 10 ($\pm$6) ppm. These average values are representative of the typical water abundance in the Martian thermosphere near a pressure level of 5×10^{-7} Pa.

3.2 Seasonal Trends

Although their is significant scatter in the data, there appears to be a sinusoidal variation in the water abundances and mixing ratios (Fig. 2), demonstrating the seasonal dependence of water in the thermosphere. To qualitatively guide the eye, we included sinusoidal curves (orange) in the top two panels of Figure 2. These curves are functions of the form

$$\rho = -A \sin(L_s) + \rho_o \tag{10}$$

where ρ is the water density or mixing ratio, A is the amplitude, L_s is solar longitude, and ρ_o is a constant. For the curves in the figure, the parameters A and ρ_o were not determined by any fitting procedure, but instead were arbitrarily chosen to simply act as a guide.

With the sinusoidal curves plotted as a visual aid, Figure 2 shows there is a consistent seasonal trend in the thermospheric water levels that is stable across more than three full Martian years. Thermospheric water levels reach a maximum around perihelion ($L_s = 251°$) and southern summer solstice ($L_s = 270°$). Note, however, the incomplete observational coverage prevents us from determining the precise solar longitude of maximum. Nonetheless, we can conclude that the data are consistent with the maximum being sometime during the period that encompasses perihelion, southern summer, and dust season. The data are also consistent with the thermospheric water levels reaching a minimum around northern summer solstice ($L_s = 90°$). This sinusoidal seasonal variation is consistent with the results of Stone20, who used observations through mid-2018 (MY34). The addition of more data in our study, which covers an additional Martian year, shows the seasonal cycle is a stable annual trend that likely occurs every martian year.

We can further investigate the seasonal trends with Figure 3, which explicitly shows the water density and mixing ratio as a function of solar longitude, with data points colored according to Mars Year. To remove some of the scatter and focus on large scale trends, we also plot medians from each individual grouping of data points. The median value for each grouping is plotted with a thick circle. The error bar represents the interquartile range. Additionally, for more context, the bottom two panels in Fig. 3 show the dust optical depths and latitudes of the individual observations.

The sinusoidal curves shown in the top two panels of Fig. 3 have the form of Equation 10, with the best-fit parameters A and ρ_o determined by fitting the grouped-median values after removing observations during significant dust storms (where the dust optical depth is greater than 0.4). Note that the use of Equation 10 assumes the solar longitudes of the minimum and maximum water levels are at 90° and 270°, respectively. The fits were not used to determine the minimum and maximum locations because the large data gaps prohibit a precise determination. Nonetheless, as discussed previously, the data are consistent with these maximum and minimum values.

The best-fit parameters for the water density are $A = 115 \pm 90$ and $\rho_o = 1400 \pm 60$. The best-fit parameters for the mixing ratio are $A = 1.3 \pm 0.7$ and $\rho_o = 11.4 \pm 0.42$. The amplitudes, A, imply the water density and mixing ratio oscillate by $\sim$10% around their mean values over a Martian year. Our derived amplitude for the mixing ratio is smaller than the amplitude derived by Stone21 who found the oscillation around the mean is $\sim$ 35%. Potential explanations for this discrepancy are the use of additional data in our study, and the slightly different methodologies. The relatively small amplitudes also imply that variations on shorter timescales are quite significant and often more prominent than the background seasonal trend.

It is interesting to compare the water levels at fixed seasons across different Mars years. In general, year-to-year water levels are more consistent during the first half of the year when atmospheric dust levels are lower and less variable. This can be seen in Figure 3 by noting the median values are more tightly grouped around the best-fit curve when L_s is less than 170°. Later in the year, when L_s is greater than 170°, the median values are more spread around the best-fit curve. Near $L_s = 240°$, the two median values (MY33 and MY35) are highly separated around the best-fit curve, with the MY33 water levels being much higher than those in MY35. This large spread may be caused by the different latitudes of the observations (MY33 are from the southern polar latitudes and MY35 are from the equatorial latitudes) or the atmospheric dust levels being higher in MY33 than in MY35. Near $L_s = 340°$, the median values are somewhat separated around the best-fit curve and the water level is higher in MY35 than in MY32 and MY33. All three of these observational periods cover equatorial latitudes so a likely explanation for the differences is the dust levels in the atmosphere, which were highest during MY35.

Although there is a background seasonal variation in the thermospheric water abundance, the individual data points can deviate significantly from ta sinusoidal curve when observations from several years are combined. This suggest that the seasonal variation can change from year-to-year and that abrupt variations on shorter time scales are also significant. In the next section, we will explore these shorter term variations by exploring how water levels respond to changing atmospheric dust loading.

3.3 Dust Correlation

Figure 4 (top) shows the explicit correlation between the water mixing ratio and the global averaged dust optical depth (Section 2). The averages of the log10 of the mixing ratios are plotted after grouping the data into dust optical depth bins of width 0.03. The Pearson correlation coefficient between the bin-averaged mixing ratios and the bin-center dust optical depths is 0.95, indicating a strong correlation. From the lowest to highest dust optical depths, the water mixing ratio increases from ∼9 to ∼60 (the highest mixing ratios and dust optical depths are from the 2018 global dust storm (Montabone et al., 2020)). Between these two extremes, the water mixing ratio steadily increases in tandem with the dust optical depth, suggesting that atmospheric dust loading is a major driver of the thermospheric water cycle. This is consistent with the observed seasonal variation of the water mixing ratio, as the dust cycle peaks during southern spring and summer when mixing ratios are highest. Further, because atmospheric dust levels differ from year-to-year, one might expect the seasonal variation in the thermospheric water level to also change from year-to-year.

A linear fit to the log10 of the mixing ratios yields

$$log_{10}(\rho) = 1.4(\pm 0.08)X + 0.82(\pm 0.02) \tag{11}$$

where ρ is the mixing ratio and X is the dust optical depth. The best-fit slope, $1.4(\pm 0.08)$, implies the relationship between mixing ratio and the dust optical depth can be approximated by a power law with a dependence that follows $\rho \propto 10^{1.4X}$.

The bottom two panels in Figure 4 show the water mixing ratio and local dust optical depth during two different time periods. Both of these periods from MY 35 are marked with white boxes in the bottom panel of Figure 2 and coincide with the onset of a regional dust storm. During the first event in June 2020, MAVEN was crossing into the northern hemisphere at low northern latitudes near 30°. The regional dust storm began just after $L_s = 220°$, when the dust optical depth began to rise. As the dust optical depth increases, the water mixing ratio also increases. This dust storm was typical for this time of year, demonstrating that the onset of typical regional dust storms leads to increased thermospheric water.

During the second event (bottom panel) in November and December 2020, a "C-type" regional dust storm (Kass et al., 2016) began just after $L_s = 315°$. MAVEN was crossing back into the southern hemisphere near equatorial latitudes. At dust storm onset, the water mixing ratio increases from ∼15 to ∼20 as the dust optical depth increases from 0.25 to 0.35. At $L_s = 325°$, the dust begins to dissipate and the mixing ratios decrease back to pre-storm values. Nonetheless, during the onset of both dust events, the water mixing ratio and dust optical depth are strongly correlated. However, each individual dust storm is somewhat unique and the response of thermospheric water might vary depending on the location with respect to the dust storm.

4 Discussion and Conclusions

MAVEN NGIMS observations allow us to infer water abundances and mixing ratios in the upper atmosphere of Mars to characterize their variability across more than

three Martian years. At a fixed atmospheric pressure level of $\sim 5\times10^{-7}$ Pa, the typical water density is 1.3 ($\pm$0.8)$\times10^3$ cm^{-3} and the typical water mixing ratio is 10 ($\pm$6) ppm. This average mixing ratio is a few times larger than that derived by Stone20, likely due to our somewhat different methodologies. Nonetheless, in agreement with Stone20, we find that water vapor is common in the upper atmosphere.

There is a seasonal variation in the thermospheric water, with higher water levels during the second half of the year – which covers southern summer, perihelion, and dust season (L_s=180°-L_s=360°) – and lower levels during the first half of the year during aphelion and non-dusty season. This is readily apparent when the water density and mixing ratio is plotted as a time series (Figure 2). However, we find it difficult to quantify how the water vapor varies as a function of solar longitude when the combining observations from three different Mars Years (Figure 3). Instead, we find it is easier to quantify how the water vapor varies as a function of the amount of dust in the lower atmosphere. This leads us to conclude that the atmospheric dust level is a strong driver of the thermospheric water.

In particular, we find the water vapor levels are consistent with a monotonically increasing dependence on the global dust optical depth (Figure 4). This supports previous work that has shown atmospheric heating from increased dust loading allows water to be transported upwards into the thermosphere without condensing (A. A. Fedorova et al., 2020; M. S. Chaffin et al., 2021; Aoki et al., 2022). Our results suggest that this process is the primary driver of thermospheric water vapor variability. Further supporting this idea is that both regional and global dust storms are clear drivers of an increase in thermospheric water .

Many questions remain about the variability of water vapor in the thermosphere such as, (1) how is the water vapor distributed with respect to local time and latitude?; (2) does the thermospheric water vapor depend on solar cycle?; and (3) how does the thermospheric water cycle affect the escape rate of hydrogen from Mars? These questions may be difficult to answer because there are limited observations after 2021 when MAVEN's orbit changed and its periapsis was raised to a higher altitude. Nonetheless, future modelling studies may use our results as constraints to explore these questions.

5 Open Research

All of the MAVEN data used in this study are available at `https://lasp.colorado.edu/maven/sdc/public/pages/datasets/ngims.html`. The dust maps are available at `http://www-mars.lmd.jussieu.fr/mars/dust_climatology/`. The derived data products will be archived on zenodo.org upon aceptance of the manuscript.

Acknowledgments

This research was conducted with the support of NASA grant 80NSSC19K1219 through the Mars Data Analysis Program, and support from the MAVEN mission through NASA headquarters. The authors thank Shane Stone and Sarah Henderson for providing useful insights.

References

Andersson, L., Ergun, R. E., Delory, G. T., Eriksson, A., Westfall, J., Reed, H., ... Meyers, D. (2015). The Langmuir Probe and Waves (LPW) Instrument for MAVEN. *Space. Sci. Rev.*, *195*, 173–198. doi: 10.1007/s11214-015-0194-3

Aoki, S., Vandaele, A. C., Daerden, F., Villanueva, G. L., Liuzzi, G., Clancy, R. T., ... Fedorova, A. A. (2022). Global Vertical Distribu-

tion of Water Vapor on Mars: Results From 3.5 Years of ExoMars-TGO/NOMAD Science Operations. *Journal of Geophysical Research: Planets*, *127*(9), e2022JE007231. Retrieved 2022-12-17, from http://onlinelibrary-wiley-com/doi/abs/10.1029/2022JE007231 (_eprint: https://agupubs.onlinelibrary.wiley.com/doi/pdf/10.1029/2022JE007231) doi: 10.1029/2022JE007231

Benna, M., Mahaffy, P. R., Grebowsky, J. M., Fox, J. L., Yelle, R. V., & Jakosky, B. M. (2015). First measurements of composition and dynamics of the Martian ionosphere by MAVEN's Neutral Gas and Ion Mass Spectrometer. *Geophys. Res. Lett.*, *42*, 8958–8965. doi: 10.1002/2015GL066146

Bhattacharyya, D., Clarke, J. T., Bertaux, J.-L., Chaufray, J.-Y., & Mayyasi, M. (2015). A strong seasonal dependence in the Martian hydrogen exosphere. *Geophysical Research Letters*, *42*(20), 8678–8685. Retrieved 2020-04-06, from http://agupubs.onlinelibrary.wiley.com/doi/abs/10.1002/2015GL065804 (_eprint: https://onlinelibrary.wiley.com/doi/pdf/10.1002/2015GL065804) doi: 10.1002/2015GL065804

Chaffin, M., Deighan, J., Schneider, N., & Stewart, A. (2017, March). Elevated atmospheric escape of atomic hydrogen from Mars induced by high-altitude water. *Nature Geoscience*, *10*(3), 174–178. Retrieved 2019-12-04, from http://www.nature.com/articles/ngeo2887 (tex.ids: chaffinElevatedAtmosphericEscape2017a, chaffinElevatedAtmosphericEscape2017b) doi: 10.1038/ngeo2887

Chaffin, M. S., Kass, D. M., Aoki, S., Fedorova, A. A., Deighan, J., Connour, K., ... Korablev, O. I. (2021, October). Martian water loss to space enhanced by regional dust storms. *Nature Astronomy*, *5*(10), 1036–1042. Retrieved 2023-01-09, from https://www.nature.com/articles/s41550-021-01425-w (Number: 10 Publisher: Nature Publishing Group) doi: 10.1038/s41550-021-01425-w

Clancy, R. T., Grossman, A. W., Wolff, M. J., James, P. B., Rudy, D. J., Billawala, Y. N., ... Muhleman, D. O. (1996, July). Water Vapor Saturation at Low Altitudes around Mars Aphelion: A Key to Mars Climate? *Icarus*, *122*(1), 36–62. Retrieved 2023-04-11, from https://www.sciencedirect.com/science/article/pii/S0019103596901086 doi: 10.1006/icar.1996.0108

Crismani, M. M. J., Villanueva, G. L., Liuzzi, G., Smith, M. D., Knutsen, E. W., Daerden, F., ... Vandaele, A. C. (2021). A Global and Seasonal Perspective of Martian Water Vapor From ExoMars/NOMAD. *Journal of Geophysical Research: Planets*, *126*(11), e2021JE006878. Retrieved 2022-12-17, from http://onlinelibrary-wiley-com/doi/abs/10.1029/2021JE006878 (_eprint: https://agupubs.onlinelibrary.wiley.com/doi/pdf/10.1029/2021JE006878) doi: 10.1029/2021JE006878

Ergun, R. E., Morooka, M. W., Andersson, L. A., Fowler, C. M., Delory, G. T., Andrews, D. J., ... Jakosky, B. M. (2015). Dayside electron temperature and density profiles at Mars: First results from the MAVEN Langmuir probe and waves instrument. *Geophysical Research Letters*, *42*(21), 8846–8853. Retrieved 2021-06-25, from http://agupubs.onlinelibrary.wiley.com/doi/abs/10.1002/2015GL065280 (_eprint: https://onlinelibrary.wiley.com/doi/pdf/10.1002/2015GL065280) doi: 10.1002/2015GL065280

Fedorova, A., Korablev, O., Bertaux, J.-L., Rodin, A., Kiselev, A., & Perrier, S. (2006). Mars water vapor abundance from SPICAM IR spectrometer: Seasonal and geographic distributions. *Journal of Geophysical Research: Planets*, *111*(E9). Retrieved 2023-04-11, from https://onlinelibrary.wiley.com/doi/abs/10.1029/2006JE002695 (_eprint: https://agupubs.onlinelibrary.wiley.com/doi/pdf/10.1029/2006JE002695) doi:

10.1029/2006JE002695

Fedorova, A., Montmessin, F., Korablev, O., Lefèvre, F., Trokhimovskiy, A., & Bertaux, J.-L. (2021). Multi-Annual Monitoring of the Water Vapor Vertical Distribution on Mars by SPICAM on Mars Express. *Journal of Geophysical Research: Planets*, *126*(1), e2020JE006616. Retrieved 2023-01-09, from http://onlinelibrary-wiley-com/doi/abs/10.1029/2020JE006616 (_eprint: https://agupubs.onlinelibrary.wiley.com/doi/pdf/10.1029/2020JE006616) doi: 10.1029/2020JE006616

Fedorova, A. A., Montmessin, F., Korablev, O., Luginin, M., Trokhimovskiy, A., Belyaev, D. A., ... Wilson, C. F. (2020, January). Stormy water on Mars: The distribution and saturation of atmospheric water during the dusty season. *Science*, *367*(6475), 297–300. Retrieved 2023-05-18, from https://www.science.org/doi/10.1126/science.aay9522 (Publisher: American Association for the Advancement of Science) doi: 10.1126/science.aay9522

Fox, J. L., Benna, M., Mahaffy, P. R., & Jakosky, B. M. (2015). Water and water ions in the Martian thermosphere/ionosphere. *Geophys. Res. Lett.*, *42*, 8977–8985. doi: 10.1002/2015GL065465

Haberle, R. M., & Jakosky, B. M. (1990). Sublimation and transport of water from the north residual polar cap on Mars. *Journal of Geophysical Research: Solid Earth*, *95*(B2), 1423–1437. Retrieved 2023-06-13, from https://onlinelibrary.wiley.com/doi/abs/10.1029/JB095iB02p01423 (_eprint: https://agupubs.onlinelibrary.wiley.com/doi/pdf/10.1029/JB095iB02p01423) doi: 10.1029/JB095iB02p01423

Halekas, J. S. (2017, May). Seasonal variability of the hydrogen exosphere of Mars: Mars Hydrogen. *Journal of Geophysical Research: Planets*, *122*(5), 901–911. Retrieved 2019-12-04, from http://doi.wiley.com/10.1002/2017JE005306 doi: 10.1002/2017JE005306

Halekas, J. S., McFadden, J. P., Brain, D. A., Luhmann, J. G., DiBraccio, G. A., Connerney, J. E. P., ... Jakosky, B. M. (2018, October). Structure and Variability of the Martian Ion Composition Boundary Layer. *Journal of Geophysical Research: Space Physics*, *123*(10), 8439–8458. Retrieved 2019-12-04, from http://doi.wiley.com/10.1029/2018JA025866 (tex.ids= halekasStructureVariabilityMartian2018a) doi: 10.1029/2018JA025866

Hunten, D. M., & McElroy, M. B. (1970, November). Production and escape of hydrogen on Mars. *Journal of Geophysical Research*, *75*(31), 5989–6001. Retrieved 2019-12-04, from http://doi.wiley.com/10.1029/JA075i031p05989 doi: 10.1029/JA075i031p05989

Jakosky, B. M. (2021). Atmospheric Loss to Space and the History of Water on Mars. *Annual Review of Earth and Planetary Sciences*, *49*(1), 71–93. Retrieved 2023-02-15, from https://doi.org/10.1146/annurev-earth-062420-052845 (_eprint: https://doi.org/10.1146/annurev-earth-062420-052845) doi: 10.1146/annurev-earth-062420-052845

Kass, D. M., Kleinböhl, A., McCleese, D. J., Schofield, J. T., & Smith, M. D. (2016). Interannual similarity in the Martian atmosphere during the dust storm season. *Geophysical Research Letters*, *43*(12), 6111–6118. Retrieved 2023-02-01, from https://onlinelibrary.wiley.com/doi/abs/10.1002/2016GL068978 (_eprint: https://agupubs.onlinelibrary.wiley.com/doi/pdf/10.1002/2016GL068978) doi: 10.1002/2016GL068978

Mahaffy, P. R., Benna, M., King, T., Harpold, D. N., Arvey, R., Barciniak, M., ... Nolan, J. T. (2015, December). The Neutral Gas and Ion Mass Spectrometer on the Mars Atmosphere and Volatile Evolution Mission. *Space Science Reviews*, *195*(1-4), 49–73. Retrieved 2019-12-04, from http://link.springer.com/10.1007/s11214-014-0091-1 doi:

10.1007/s11214-014-0091-1

Matta, M., Withers, P., & Mendillo, M. (2013, May). The composition of Mars' topside ionosphere: Effects of hydrogen: HYDROGEN EFFECTS ON MARTIAN IONOSPHERE. *Journal of Geophysical Research: Space Physics*, *118*(5), 2681–2693. Retrieved 2019-12-04, from http://doi.wiley.com/10.1002/jgra.50104 doi: 10.1002/jgra.50104

McElroy, D., Walsh, C., Markwick, A. J., Cordiner, M. A., Smith, K., & Millar, T. J. (2013, February). The UMIST database for astrochemistry 2012. *Astronomy & Astrophysics*, *550*, A36. Retrieved 2022-12-22, from https://www.aanda.org/articles/aa/abs/2013/02/aa20465-12/aa20465-12.html (Publisher: EDP Sciences) doi: 10.1051/0004-6361/201220465

Montabone, L., Forget, F., Millour, E., Wilson, R., Lewis, S., Cantor, B., ... Wolff, M. (2015, May). Eight-year climatology of dust optical depth on Mars. *Icarus*, *251*, 65–95. Retrieved 2019-12-04, from https://linkinghub.elsevier.com/retrieve/pii/S0019103515000044 doi: 10.1016/j.icarus.2014.12.034

Montabone, L., Spiga, A., Kass, D. M., Kleinböhl, A., Forget, F., & Millour, E. (2020). Martian Year 34 Column Dust Climatology from Mars Climate Sounder Observations: Reconstructed Maps and Model Simulations. *Journal of Geophysical Research: Planets*, *125*(8), e2019JE006111. Retrieved 2020-10-27, from http://agupubs.onlinelibrary.wiley.com/doi/abs/10.1029/2019JE006111 (_eprint: https://onlinelibrary.wiley.com/doi/pdf/10.1029/2019JE006111) doi: 10.1029/2019JE006111

Montmessin, F., Smith, M., Langevin, Y., Mellon, M., & Federova, A. (2017). The water cycle. In *The Atmosphere and Climate of Mars.* Cambridge University Press.

Schunk, R. W., & Nagy, A. F. (2009). *Ionospheres* (Second ed.). New York: Cambridge University Press.

Smith, M. D., Wolff, M. J., Clancy, R. T., & Murchie, S. L. (2009). Compact Reconnaissance Imaging Spectrometer observations of water vapor and carbon monoxide. *Journal of Geophysical Research: Planets*, *114*(E2). Retrieved 2023-04-11, from https://onlinelibrary.wiley.com/doi/abs/10.1029/2008JE003288 (_eprint: https://agupubs.onlinelibrary.wiley.com/doi/pdf/10.1029/2008JE003288) doi: 10.1029/2008JE003288

Stone, S. W., Yelle, R. V., Benna, M., Elrod, M. K., & Mahaffy, P. R. (2018, November). Thermal Structure of the Martian Upper Atmosphere From MAVEN NGIMS. *Journal of Geophysical Research: Planets*, *123*(11), 2842–2867. Retrieved 2019-12-04, from http://doi.wiley.com/10.1029/2018JE005559 doi: 10.1029/2018JE005559

Stone, S. W., Yelle, R. V., Benna, M., Lo, D. Y., Elrod, M. K., & Mahaffy, P. R. (2020, November). Hydrogen escape from Mars is driven by seasonal and dust storm transport of water. *Science*, *370*(6518), 824–831. Retrieved 2021-02-26, from http://science.sciencemag.org/content/370/6518/824 (Publisher: American Association for the Advancement of Science Section: Research Article) doi: 10.1126/science.aba5229

Villanueva, G. L., Liuzzi, G., Crismani, M. M. J., Aoki, S., Vandaele, A. C., Daerden, F., ... NOMAD TEAM (2021, February). Water heavily fractionated as it ascends on Mars as revealed by ExoMars/NOMAD. *Science Advances*, *7*(7), eabc8843. Retrieved 2023-05-18, from https://www.science.org/doi/10.1126/sciadv.abc8843 (Publisher: American Association for the Advancement of Science) doi: 10.1126/sciadv.abc8843

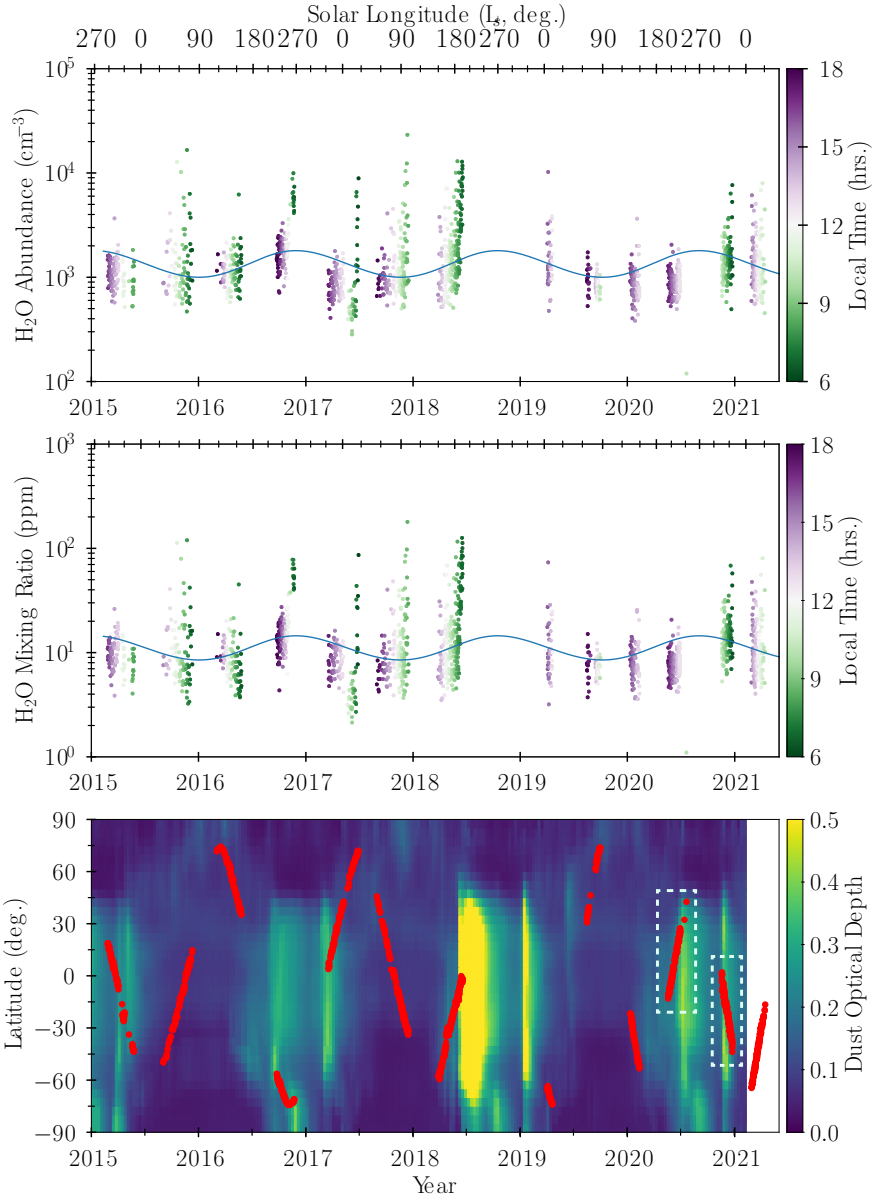

Figure 2. Derived thermospheric water abundances (top) and mixing ratios (middle). The bottom panel shows dust optical depth maps with the locations of the MAVEN observations shown in red. The dust optical depth data does not extend beyond early 2021. The two white boxes mark the regional dust storms that are analyzed in Section 3.3. The orange curves are sine functions that qualitatively demonstrate the seasonal dependence of water in the thermosphere.

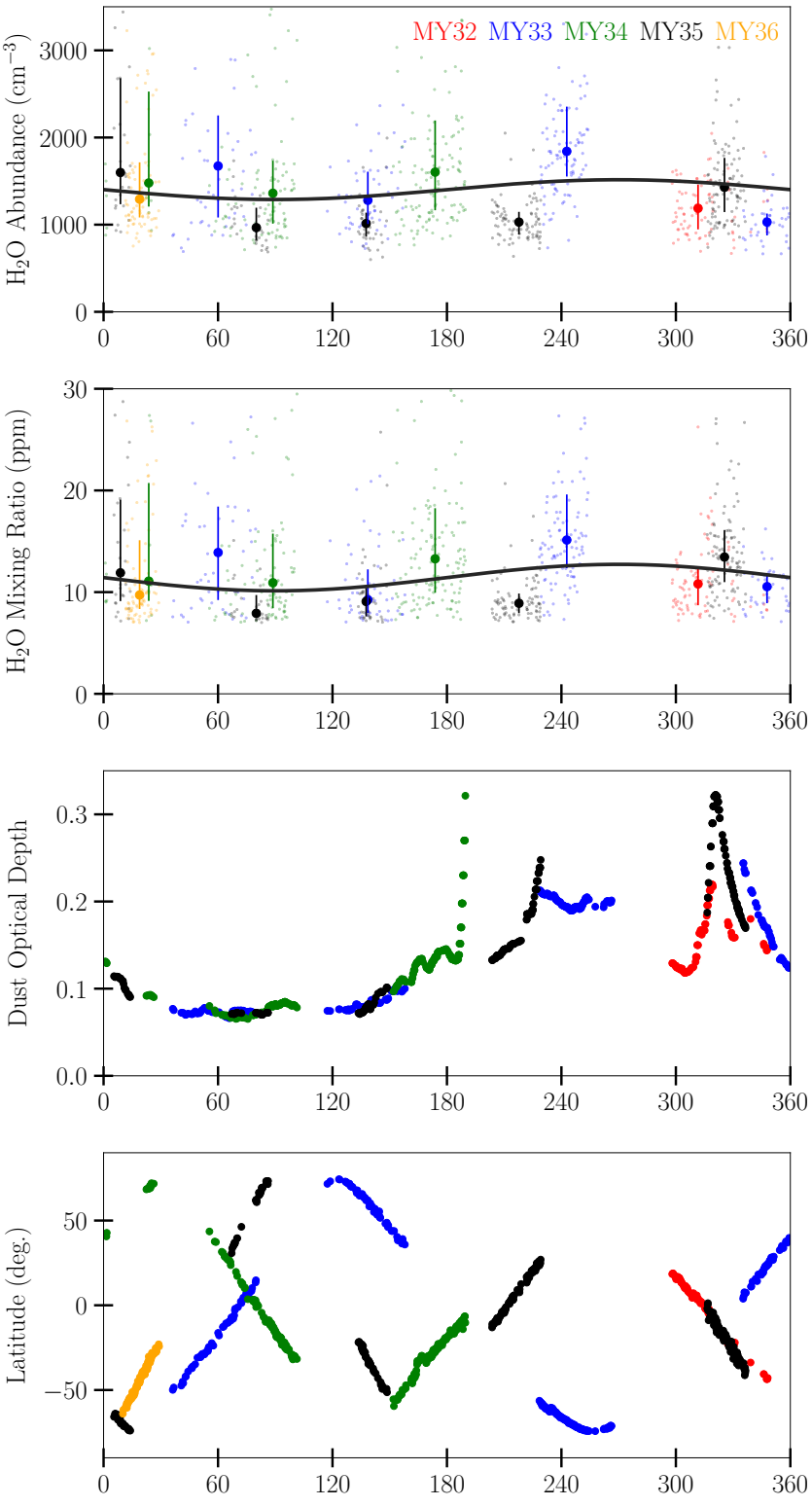

Figure 3. Thermospheric water abundance and mixing ratio as a function of solar longitude (top two panels). The values from each orbit are shown with tiny circles, the grouped-median values are shown with large circles, and the error bars encompass the interquartile range. Colors mark the different Mars Years and the black curves are sinusoidal fits to the median values. The bottom two panels show the dust optical depth and latitude, respectively.

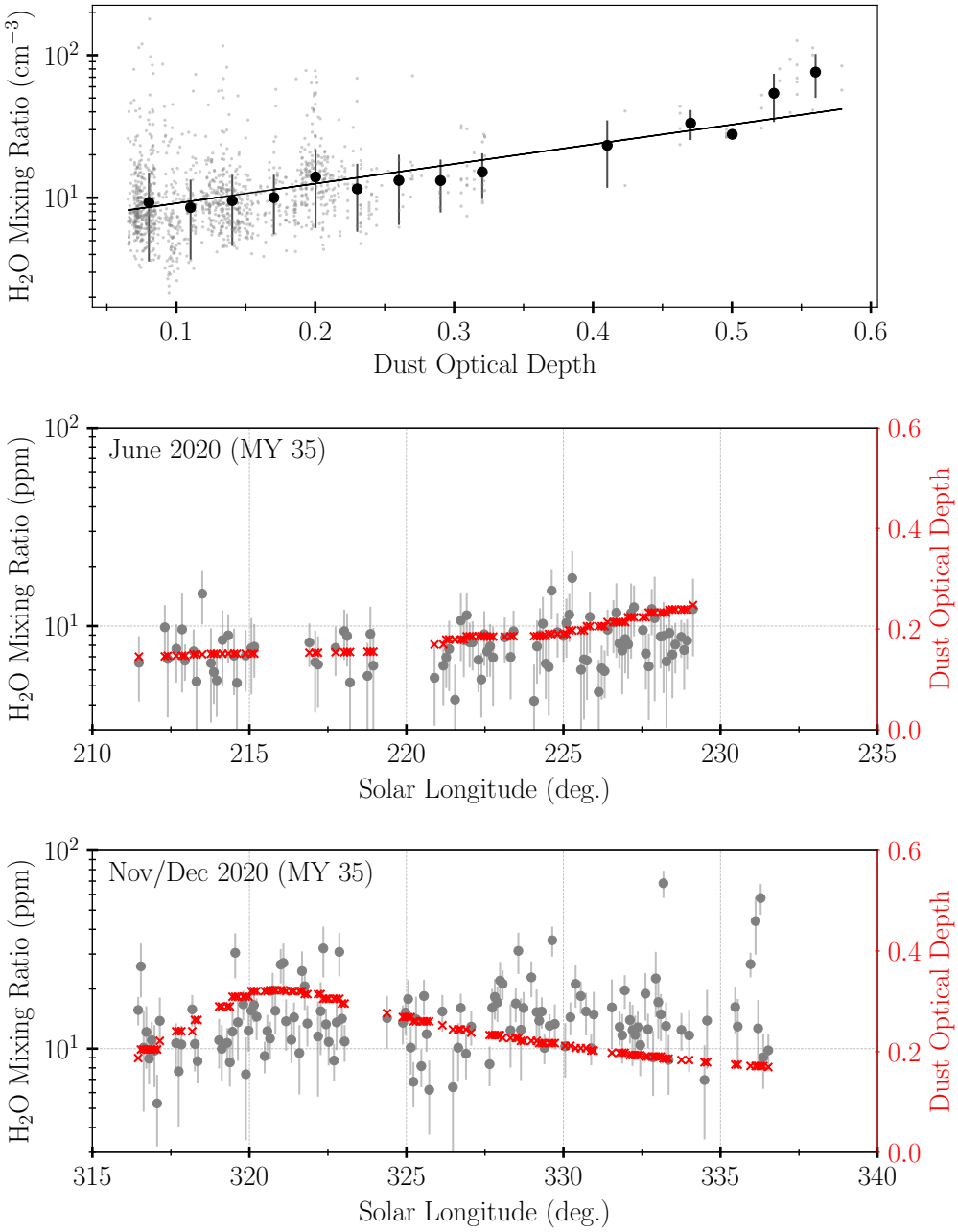

Figure 4. The top panel shows the thermospheric water mixing ratio as a function of global-averaged column dust optical depth. Small circles show the individual data points, large circles show the average values after separating the data into dust optical depth bins. The black line is a best-fit to the binned averages. The middle panel and bottom panel each show the mixing ratio and dust optical depth during a regional dust storm in MY 35.